Defect formation and migration in MAlB (M = Mo, W) and N_2AlB_2 (N = Cr, Fe): A first-principles study

Salawu Omotayo Akande and Deniz Çakır*
Department of Physics and Astrophysics, University of North Dakota, Grand Forks, North Dakota 58202, USA

(Received 11 January 2023; revised 5 April 2023; accepted 25 April 2023; published 18 May 2023)

The exceptional properties of MAB phases (where M = transition metal, A = aluminum, and B = boron) make them a promising option for various applications. However, their usage in most fields requires an understanding of the defect formation and migration processes, which can aid in designing durable and functional materials. Through density functional theory calculations, we investigated the stability and mobility of the most prominent point and extended defects in MAlB (where M = Mo and W) and N_2AlB_2 (where N = Cr and Fe) MAB phases under different chemical conditions. Our findings indicate that V_B/N_{Al} is the easiest defect to form under M/N-rich conditions. We observed that vacancy and antisite defects form more easily than interstitial ones in all studied systems. We also investigated different extended structural defects and stacking faults and revealed the stability of relevant compositional defects and tilt/rotational boundaries in MAlB and N_2AlB_2. Our results suggest that these systems can likely be synthesized by tuning the experimental conditions. We additionally observed grain boundary formation in N_2AlB_2 and compared our findings with relevant experiments.

DOI: 10.1103/PhysRevMaterials.7.053610

I. INTRODUCTION

The atomically laminated layered ternary transition metal borides, the so-called MAB phase (where M = transition metal, A = aluminum, and B = boron) in analogy to the well-studied similar compounds (known as the MAX phase), have been shown to exhibit promising properties and have found application in various fields [1]. They have been reported to have a high melting point, high strength, high decomposition temperature, and high-temperature diffusion barrier [2,3]. They are known to possess close resemblance to their binary borides and are precursors toward the formation of quasi-two-dimensional MBene materials [3]. Generally speaking, the structure of the MAB phase can be described as consisting of boron atoms coordinated by six transition metal atoms. The MAB phase typically adopts the orthorhombic crystal structure, which comprises M-B blocks made up of face-sharing trigonal prisms that are separated by Al layer(s) [4]. Recently, a hexagonal symmetry has also been reported for Ti_2InB_2 [5]. This discovery has opened a route for further probing of the likelihood of expanding the composition and crystal structure space of the MAB phases [6].

Recently, the MAB phases have been considered as materials for various applications in aerospace, mining, nuclear reactor, and energy applications that require high-performance materials capable of performing under very demanding scenarios, especially at high temperatures [2,7]. Moreover, these materials should be capable of withstanding chemical attacks, high-energy radiation, and mechanical wear and tear [8]. Some of the traits needed to realize the aforementioned applications have been reported for the MAB phases. Specifically, MoAlB has been found to be stable up to 1600 °C owing to the formation of Al_2O_3 scales that serve as a protective covering [9]. Similarly, there have been reports for crack healing [8], grain delamination, and crack deflection [10–12]. However, there is a need for synthesis at a lower temperature if the potentials of these materials are to be realized. While the radiation tolerance capabilities of the MAX phases have been established, it is expected that the similarity in structure between both phases could translate to this capability in the MAB phases [13]. Recent studies in fact showed that MoAlB does not suffer from the radiation-induced cracking often observed in the MAX phases, although radiation-induced amorphization was reported [8,14,15]. This suggests that MAB phases might be promising materials for applications that involve radiation. Buoyed by the impeccable performance of the MoAlB, there has been increased research in similar materials. For example, the WAlB and other similar materials have been attracting interest and efforts have been made to characterize them. These efforts have been hampered by the difficulty in the synthesis of the bulk form of these kinds of materials [8,16]. Furthermore, Ade and Hillebrecht's report on the synthesis and growth of Cr-based MAB phases offers more insight into the behavior of this class of material [3]. They reported similarities of the MAB phases with orthorhombic binaries and suggested a structure-property relationship.

The applicability of the materials for various purposes is heavily determined by the behavior of defects. A comprehensive understanding of defect energetics is important to improve material performance [4,13]. This is particularly important for the MAB phases, in addition to point defects, as there have been reports of deviations from the pristine crystal structure evidenced by the appearance of twist/twin boundaries and stacking-fault-like defects in some of the

*deniz.cakir@und.edu

MAB phases synthesized [2,13]. Specifically, these investigations have revealed the presence of structural defects like twist boundaries, intergrown compositional defects, and twin boundaries. The stability of materials is certainly affected by these defects, which can be thermally induced or formed during irradiation. A detailed characterization of the defect behavior is lacking for several compounds in the MAB phase, especially the stability of the deviations from pristine MAB reported experimentally. Moreover, the defects in crystals have been the subject of intense investigations that are useful in understanding the thermodynamical stability, decomposition into competing/secondary phases, and mass transport. Efforts have been made to calculate the defect formation energy in the MAX phase and some compounds crystallizing in the MAB phase [8,13]. The findings have helped not only in providing insight into the applicability of these materials but also valuable insight on how to improve their material properties [17].

Density functional theory (DFT) with appropriate exchange-correlation functionals is a reliable tool to characterize different properties of materials including defect energetics [9]. It is capable of predicting the stability of materials and is often employed for calculating properties that are either not possible experimentally or too expensive to investigate. The stability of different MAX and MAB phases has been studied using DFT calculations [13,18–22]. Attempts have also been made to investigate defect energetics in some of the MAB phases [13,14]. Previously, using DFT calculations, the defect recovery process in Fe_2AlB_2 was shown to be very effective [9]. One of the important factors that determine the reliability of the model used to calculate the defect formation energy is the size of the simulation cell adopted. Hence, choosing a large supercell is essential to minimize defect-defect interactions which normally contribute to an inaccurate prediction of defect energetics. This is particularly important in order not to incorrectly estimate the defect energetics.

This work aims to calculate the formation energy of various defects and predicts the most likely types of point and extended defects found in the MAB phases using first-principles calculations. Different sizes of supercells were adopted in order to unravel the role of defect-defect interaction on the energetics calculated. We also characterized the stability of structural and compositional defects, which have been experimentally reported to form in each of the systems under investigation. The migration of the most prominent point defects was investigated. Finally, the formation of grain boundaries was searched by calculating grain boundary formation energies. Although this work focuses on the MAB phase, the inferences drawn from this investigation will aid in understanding other materials used for similar applications.

II. COMPUTATIONAL DETAILS

We employed first-principles calculations based on density functional theory (DFT) as implemented in the Vienna *ab initio* simulation package (VASP) [23–26]. The Perdew-Burke-Ernzerhof flavor of the generalized gradient approximation was employed for all calculations [27,28]. The electron-ion interactions were considered by employing the projected augmented wave (PAW) method [29,30]. Our choice of functional was found to reproduce experimental results remarkable well. Additionally, we previously demonstrated by assessing various exchange-correlation functionals including GGA-PBE, GGA-PBE + U, SCAN, and dynamical mean field theory that the GGA-PBE functional is capable of investigating key properties, such as the magnetic ground state, magnetic moments, and lattice parameters, of MAB phases despite the existence of transition metals [22,31]. We studied MAlB (M = Mo, W) with the space group of *Cmcm* and N_2AlB_2 (M = Cr, Fe) with the space group of *Cmmm*, see Figs. 1(a) and 1(b), with two different supercell sizes, namely a $2 \times 2 \times 2$ cell (96 atoms for MAlB, 80 atoms for N_2AlB_2) and a $4 \times 4 \times 1$ cell (192 atoms for MAlB, 160 atoms for N_2AlB_2). The lattice parameter and atomic positions were fully relaxed with a Monkhorst-Pack scheme employed for the integration of the Brillouin zone. The k mesh was chosen according to the size of the simulation cell. The kinetic energy cutoff of the plane wave basis was set to 520 eV. The energy convergence criterion was set to 10^{-6} eV, while the force convergence criterion of the ionic steps was 10^{-2} eV/Å. In order to obtain accurate structural parameters, the lattice parameters and internal coordinates were fully optimized. The climbing image nudged elastic band (CI-NEB) method was applied to construct the minimum energy paths for the migration of different point defect types [32,33].

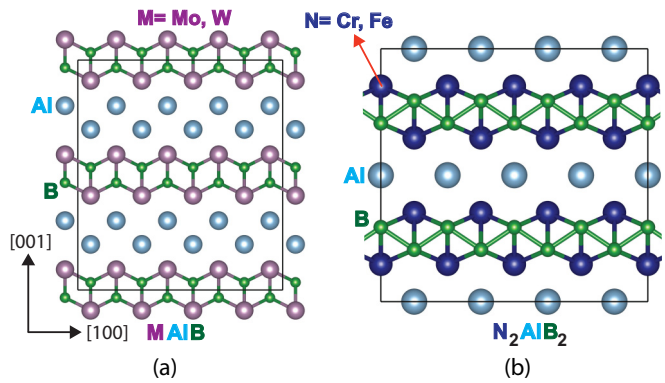

FIG. 1. Crystal structure of optimized $4 \times 4 \times 1$ supercell of (a) MAlB and (b) N_2AlB_2 system.

III. RESULTS AND DISCUSSION

A. Point defects

MAlB (where M = Mo and W) and N_2AlB_2 (where N = Cr and Fe) MAB phases crystallize in the orthorhombic crystal structure as denoted in Fig. 1. The calculated lattice parameters are presented in Table I and in agreement with the available experimental results.

After obtaining the structural properties of the defect-free systems, we proceeded to calculate the energy of formation of the different point defect types in the systems under investigation. Defects in materials are important as they control the various material properties [35]. In each system, we considered all symmetrically nonequivalent lattice sites for the formation of the vacancies, interstitial, and antisite defects and we only reported the most stable defect configurations.

TABLE I. Calculated lattice parameters (in Å) and comparison with available experimental results.

	This work	Experiment [1,3,34]
MoAlB	$a = 3.22$	3.20
	$b = 14.11$	13.92
	$c = 3.12$	3.09
WAlB	$a = 3.22$	3.20
	$b = 14.01$	13.91
	$c = 3.11$	2.91
Cr_2AlB_2	$a = 2.98$	2.94
	$b = 11.13$	11.05
	$c = 3.02$	2.97
Fe_2AlB_2	$a = 2.910$	2.9287
	$b = 11.11$	11.0313
	$c = 2.92$	2.869

To calculate the energy of the formation of these defects, it is essential to establish a valid chemical potential range. The chemical potentials are governed by equilibrium conditions as well as the restriction on the appearance of the unwanted secondary and/or competing phases. The latter used here were obtained from the Materials Project [36], Springer Materials [37], and previously published works on the MAB phases [38,39]. In order to ensure stable MAlB and N_2AlB_2 compounds at equilibrium, the chemical potentials of the constituents in each compound need to satisfy the following conditions:

$$\Delta\mu_{\mathrm{M}} + \Delta\mu_{\mathrm{Al}} + \Delta\mu_{\mathrm{B}} = \Delta\mu_{E_{f(\mathrm{MAlB})}}, \tag{1}$$

$$2\Delta\mu_{\mathrm{N}} + \Delta\mu_{\mathrm{Al}} + 2\Delta\mu_{\mathrm{B}} = \Delta\mu_{E_{f(\mathrm{N_2AlB_2})}}. \tag{2}$$

Here $\Delta\mu_{\mathrm{M}}$, $\Delta\mu_{\mathrm{Al}}$, $\Delta\mu_{\mathrm{B}}$, and $\Delta\mu_{\mathrm{N}}$ are the relative chemical potentials of M, Al, B, and N, respectively. In addition, $\Delta\mu_i = \mu_i - \mu_i^o$, and μ_i^o is the atomic chemical potential in the elemental solid state of the atom involved. To prevent the formation of competing phases, the formation energy of MAlB and N_2AlB_2 needs to be lower than that of the competing phases. Taking this and the different equations for the competing phases into consideration, we obtained the stability limits for each system and show them in Fig. 2. The competing phases and the formalism culminating in the stability limits adopted for all the compounds are presented in the Supplemental Material (see Figs. S1–S4) [40]. The points mark the regions where the secondary phases cannot be formed, and are labeled as points I–VI in the stability diagram in Fig. 2. Points I and VI show M- and N-rich conditions, while points II and III depict Al-rich conditions. Boron-rich conditions are marked at points IV and V. Having established a stability limit for the chemical potential, we computed the formation energies for the different defect types using the following expression:

$$E_f = E_{\mathrm{defected}} - E_{\mathrm{pristine}} + \sum n_i\mu_i, \tag{3}$$

where E_{defected} and E_{pristine} are the total energies of a supercell with and without the defect, respectively. n_i and μ_i are the numbers of atoms involved in the defect formation and their chemical potentials, respectively. The defects considered in this work include M, N, Al, and B vacancies and interstitials. We also included all possible antisite combinations for each system. First, we calculated the defect formation energies for $2 \times 2 \times 2$ and $4 \times 4 \times 1$ supercell structures to assess the effect of simulation cell dimensions on the defect formation energies. Figure 3 denotes the results for MoAlB, where Mo, Al, and B vacancies were selected. The first observation is that the defect formation energies markedly depend on the chemi-

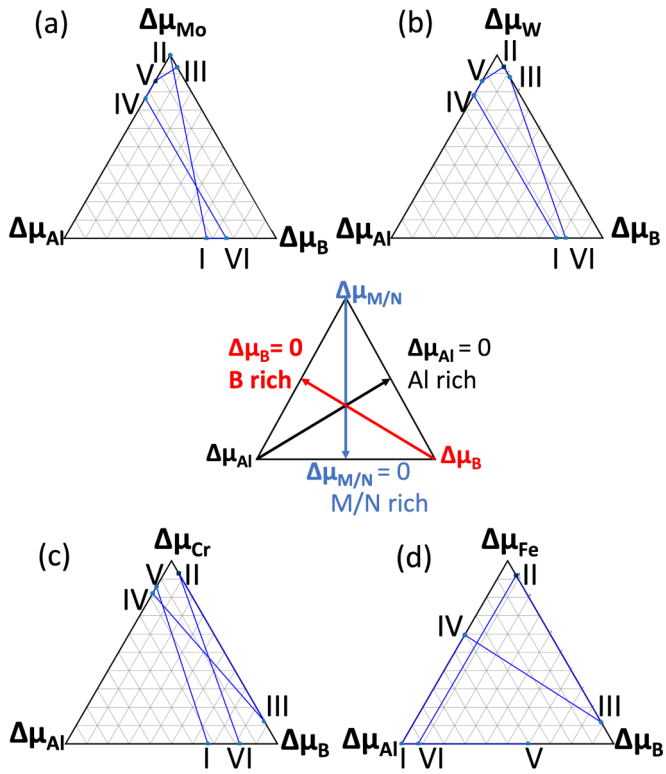

FIG. 2. Stability diagram for (a) MoAlB, (b)WAlB, (c) Cr_2AlB_2, and (d) Fe_2AlB_2.

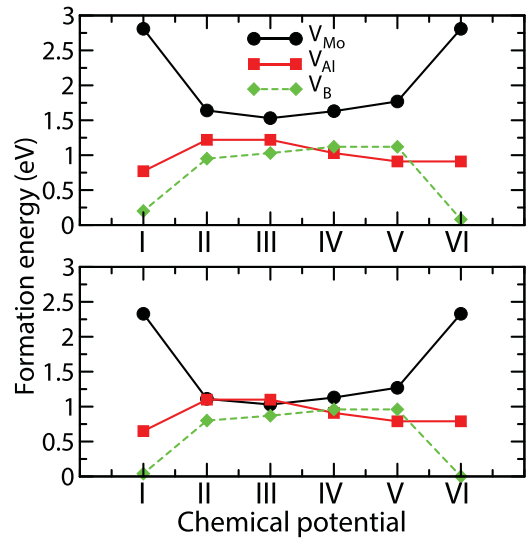

FIG. 3. Vacancy formation energies in MoAlB calculated using a $2 \times 2 \times 2$ (bottom) and a $4 \times 4 \times 1$ simulation cell (top).

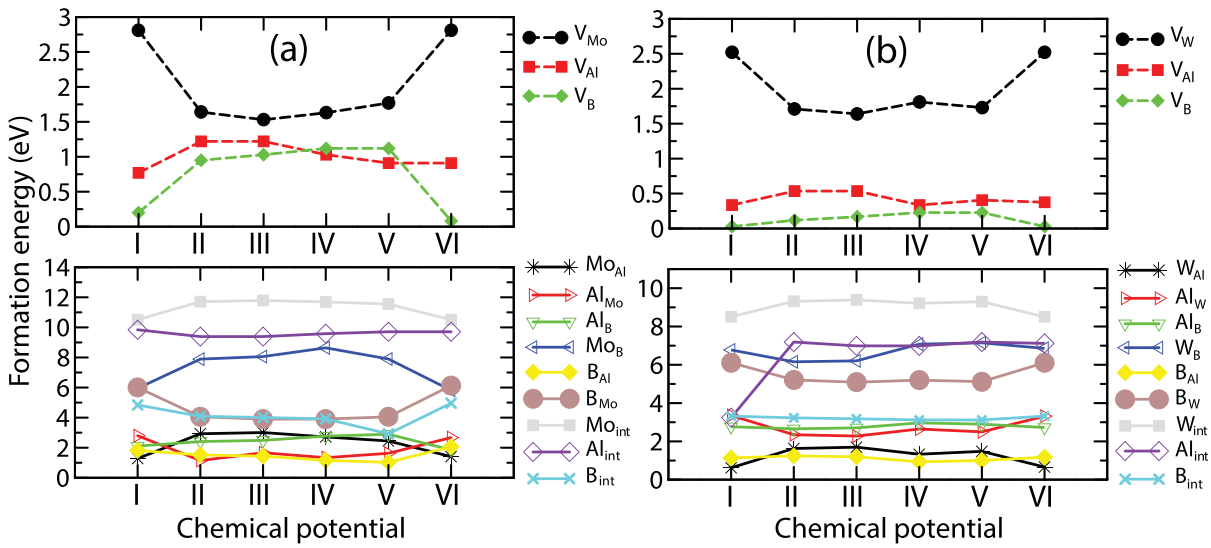

FIG. 4. Calculated defect formation energies for (a) MoAlB and (b) WAlB as a function of the atomic chemical potential. The first row is the vacancy formation energies and the second row shows the antisite and interstitial formation energies.

cal potential. In order to determine the effect of defect-defect interaction, we calculated the defect formation energy using a $4 \times 4 \times 1$ supercell. We found that the $2 \times 2 \times 2$ supercell overestimates the defect formation energy by up to 0.5 eV, as seen in Fig. 3. Therefore, in the rest of the paper, we only discuss results obtained using the $4 \times 4 \times 1$ simulation cell to elucidate the properties of isolated defects.

The defect formation energy for MAlB as a function of the stability limits established above is shown in Fig. 4. From the computed defect formation energies for MoAlB, we observed that at point I (i.e., Mo-rich), V_B has a lower formation energy than V_{Mo} and V_{Al}. From point I to II, the defect formation energy increases for both V_B and V_{Al}, while we observed a decrease for V_{Mo}. At point II (i.e., Al-rich), the difference in the defect formation energies for all vacancies reduces and becomes even smaller as we move to points II–IV, where the defect formation energies are not too different. At point V (i.e., B-rich), the difference in the formation energy begins to increase again with the defect formation energy of V_{Mo} to be increased sharply until it reaches a maximum value at point VI. Conversely, the defect formation energy of V_B reduces to a minimum value, and the value for V_{Al} remains almost unchanged. We found a similar behavior for WAlB [see Fig. 4(b)]. Noteworthy, however, is that the defect formation energy is generally lower in WAlB than in MoAlB, although the defect formation energies for V_{Mo} and V_W still remain very high in both systems. That V_B at rich M is very small shows the impact of the chemical potential on the defect formation energetics in MAlB. Also, the formation energy of V_B is generally very low.

The antisite and interstitial defects are shown in the second row of Figs. 4(a) and 4(b). The formation energies can be roughly divided into three main groups. The first group comprises the Mo/W interstitial defects. We found that the M_{int} are the most difficult to form of all the point defect types considered irrespective of the chemical potential. The second group includes Al_{int}, B_W, and W_B, and this group forms the next most difficult defects to form. From the second group, we begin to observe the dependence of the formation energy on the chemical potential. This behavior is particularly more pronounced in the third group which comprises M_{Al}, Al_M, and B_{Al}. The most favorable defect types in this group and the value of the defect formation energy depend heavily on the stability of the chemical potential. For MAlB, we found that the M interstitial defects are very difficult to form with formation energy larger than 10 eV in both systems, which is attributed to the size of metal atoms relative to the interstitial sites. This observation is valid irrespective of the atomic chemical potential. The formation of metal interstitials has been found experimentally to be detrimental to the defect recovery process and our calculations have lent credence to this as we have shown the prohibitive cost of their formation. The more favorable defects to form in this category are the Mo_{Al}, Al_{Mo}, B_{Al} antisites.

For N_2AlB_2, the defect formation trend is different from those described above for the MAlB. Specifically, unlike in MAlB where V_M is the most difficult vacancy to form, the V_{Al} is the most difficult vacancy to form in N_2AlB_2. For Fe_2AlB_2, the formation of V_{Al} is the hardest and it depends on the atomic chemical potential with its formation more favored under the Fe-rich conditions. Although the V_B defect is still the most favorable vacancy defect in Cr_2AlB_2 and Fe_2AlB_2, there is a competition with V_{Cr} notably under the Al-rich condition (point II) in Cr_2AlB_2 and rich Al/B condition (points II and IV) in Fe_2AlB_2. Similar to the MAlB systems, we found that the metal interstitial defects are the most difficult ones to form irrespective of the atomic chemical potential in N_2AlB_2. However, the formation energies are much lower (see Fig. 5). While Cr_{Al} was calculated to be the most favorable to form in Cr_2AlB_2, the values obtained for Fe_2AlB_2 show that Al_B and Fe_{Al} antisites are more favorable depending on the atomic chemical potential. The defect formation energy of Cr_{Al} is very small and calculated as the lowest energy defect in Cr_2AlB_2.

The trend in the defect formation energies observed for MAlB and N_2AlB_2 has previously been linked to the

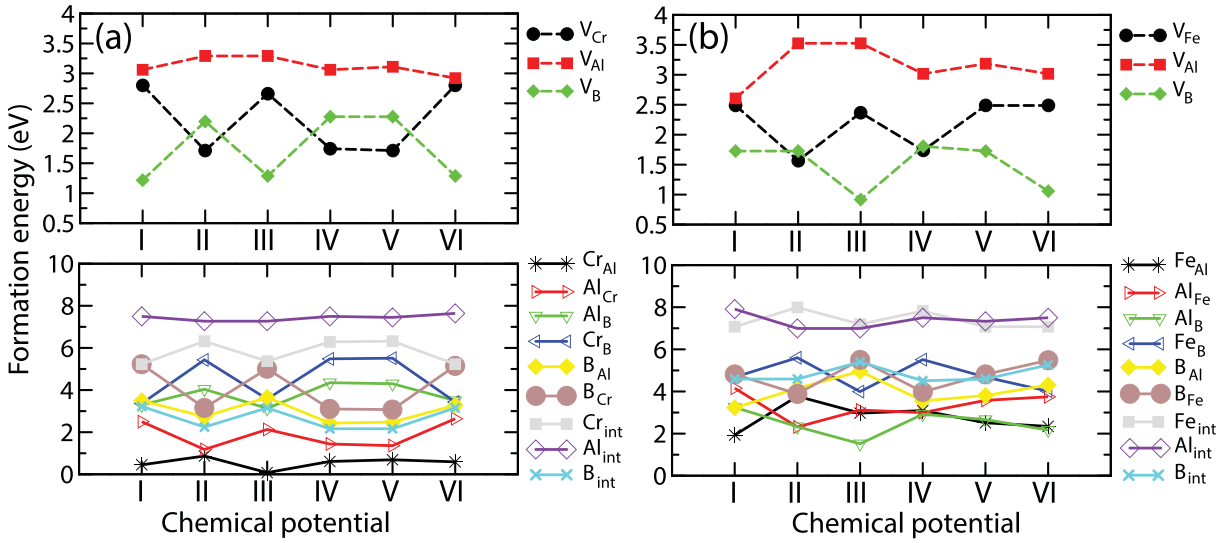

FIG. 5. Calculated defect formation energies for (a) Cr_2AlB_2 and (b) Fe_2AlB_2 as a function of the atomic chemical potential. The first row is the vacancy formation energies and the second row shows the antisite and interstitial formation energies.

crystal structure of the MAB phases [41]. Our investigation clearly shows that in addition to the crystal structure and the number of Al layers, the type of the metal determines the defect energetic in the MAB compounds. Moreover, Izabela and co-workers reported that the order of tolerance to defects increases as the number of B network and Al layers increases [14]. Understanding the order of tolerance in these materials is the key to gaining a deeper insight into the recovery processes. Further analysis of the energetics revealed that, generally, the vacancies and antisite defects are easier to form in each of the systems under investigation. Interstitials, on the other hand, are much more difficult to form, especially metal interstitials. The vacancy formation energies are quite close to the antisite formation energies and both defects could compete or interact while these materials are in operation.

To comprehend the variations in the defect formation energies of MoAlB and WAlB, we explored the potential factors that can impact the defect formation energetics in both systems. Initially, we observed comparable alterations in volume and local structural relaxation during defect formation. Specifically, we determined a difference of 0.04%, 0.16%, and 0.10% in volume expansion between MoAlB and WAlB for the formation of M, Al, and B vacancies, respectively. Subsequently, we examined the chemical bonding in the systems under investigation and evaluated the covalent bond strength in the materials using integrated crystal orbital Hamilton population (ICOHP) analysis. To do this, we employed the Local Orbital Basis Suite toward Electronic-Structure Reconstruction (LOBSTER) code [42–44]. In the Supplemental Material [40], Tables S3 and S4 show the calculated ICOHP values for various M/N-Al, M/N-B, M/N-M/N, Al-B, and B-B bonds in MAlB and N_2AlB_2. As shown in Tables S3 and S4, B-B and M-B bonds are stiffer than all other bond types. Comparison of the ICOHP values for MoAlB and WAlB shows that WAlB exhibits slightly stronger covalent character. Throughout the chemical potential range we examined, the formation energies of antisite defects M/N_{Al} and $Al_{M/N}$ are relatively lower. This trend is associated with smallest ICOHP values of M/N-Al bonds in the respective systems. However, the calculated ICOHP values alone do not provide a comprehensive understanding of the defect energetics across the entire chemical potential range studied. At this point, we should note that the defect energetics in MAB phases are likely influenced by a combination of covalent, ionic, and metallic chemical bonding. Further analysis reveals that the disparity in the defect formation energies between MAlB and N_2AlB_2 primarily stems from the chemical potentials utilized in the calculation of the defect formation energies.

B. Extended structural defects and stacking faults

Experiments showed that structural defects are inherent in the MAB phases [13,34,45]. Using analytical aberration-corrected scanning transmission electron microscopy, Hultman *et al.* confirmed the existence of deviations from pristine structures such as a tilted boundary, a twisted boundary, and a number of stacking faults observed in some of the MAB phases [34]. Similarly, Christiana *et al.* demonstrated the presence of these structural deviations and opined that they might have a strong impact on the feasibility of Al deintercalation and consequently in the formation of 2D MBenes [13]. They also reported that these stacking faults comprise layered domains. For MAlB, we considered eight different stacking faults. This includes a scenario where an MB layer resides next to another one with two missing Al layers between them (here referred to as Al-missed), which resembles orthorhombic MB; see Fig. 6(a). In Fig. 6(b), we represent a compositional defect (labeled as cd), where two adjacent Al layers are substituted by a twisted MB layer to mimic a bulk MB compound with space group $I4_1/amd$. Those two structural defects are included since bulk MB is a competing phase for the MAB compounds. Compositional defects, where the relative concentrations of Mo and B are varied, were also considered. Here, we represented such variations as cd-1 (with M_4B_5), cd-2 (with M_4B_6), and cd-3 (with M_3B_4); see

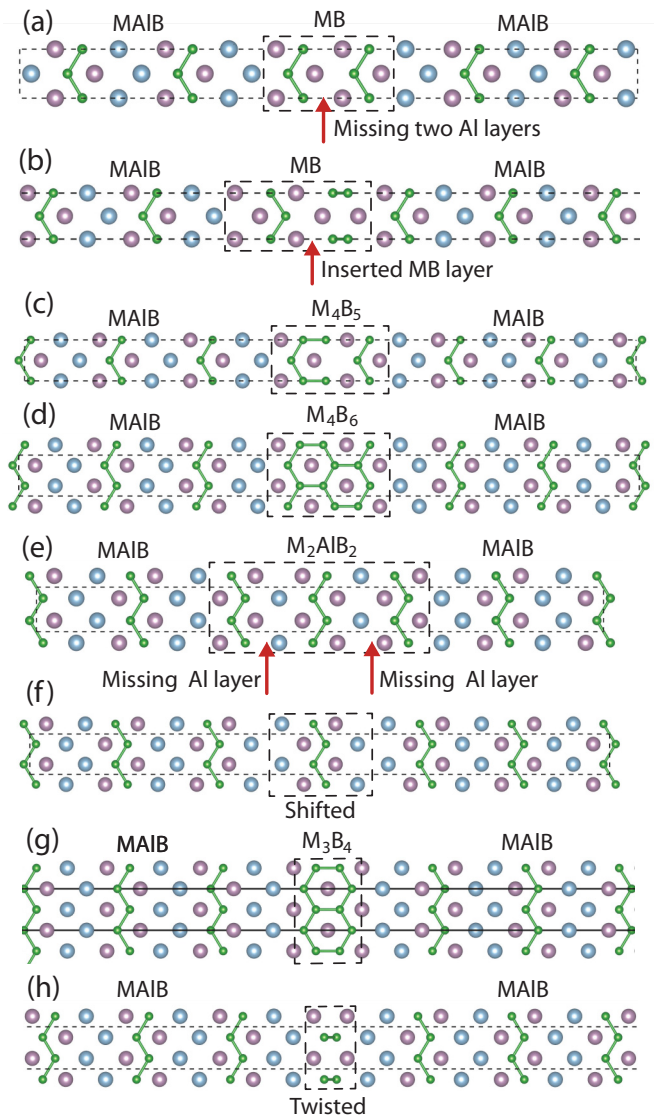

FIG. 6. Schematics of the structural defects in MAlB showing (a) Al-missed, (b) inserted, (c) cd-1, (d) cd-2, (e) M_2AlB_2-type defect, (f) shifted, (g) cd-3, (h) twist boundary.

Figs. 6(c), 6(d), and 6(g). Several previous works reported the presence of twist boundaries in MAlB-type MAB phases [34,45]. The twist fault is as shown in Fig. 6(h). A stacking fault with the same atomic layer sequence as the N_2AlB_2-type MAB phase is represented as M_2AlB_2 in Fig. 6(e). Lars *et al.* concluded that if synthesized it would represent a new M-Al-B phase [2]. Figure 6(f) shows a stacking fault where a M_2AlB_2 subunit is shifted by a half lattice parameter along the [010] direction.

For N_2AlB_2, owing to the ordering of the N and B atoms in the N-B sublattice being similar to the bulk NB (for example orthorhombic CrB structure with *Cmcm* space group) adopted during synthesis, it is worth considering the formation of the NB embedded into N_2AlB_2. We considered two variations of this scenario, namely NB-1 and NB-2, as denoted in Figs. 7(a) and 7(b). The two other configurations considered in this category include the rotation of one layer of the NB layer (NB-rot-1) around the [001] direction, see Fig. 7(c), and the

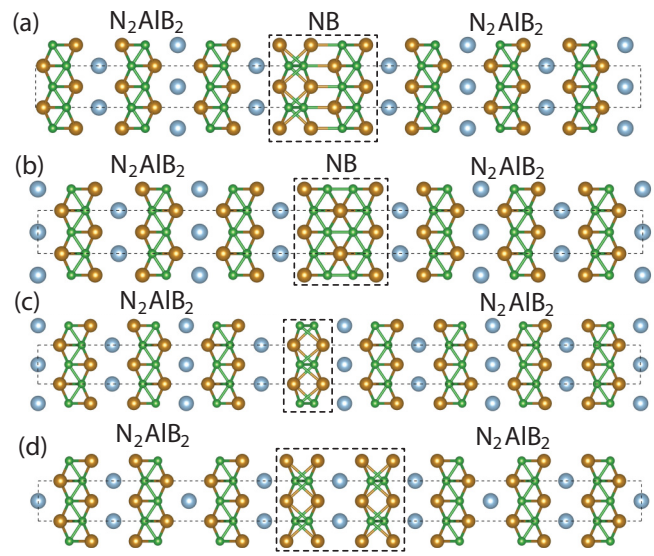

FIG. 7. Schematics of the structural defects in N_2AlB_2 showing (a) NB-1, (b) NB-2, (c) NB-rot-1, (d) NB-rot-2.

rotation of two adjacent NB layers (NB-rot-2) around the [001] direction followed by a half lattice constant translation; see Fig. 7(d).

The stability of these structural deviations can be determined by quantifying their formation enthalpy. We modeled these systems by replicating the features of these defects using supercell structures. To this end, we calculated the formation energies of the different complex defect types that have been identified. The formation energy per atom is calculated using the following expression [13]:

$$E_f = \left[E_{M_xAl_yB_z} - (xE_M + yE_{Al} + zE_B)\right]/(x + y + z). \quad (4)$$

Here $E_{M_xAl_yB_z}$ is the energy of the system with the complex defect, and E_M, E_{Al}, and E_B are the bulk energies of M (Mo/W/Cr/Fe), Al, and B, respectively. x, y, and z are the number of corresponding atoms in the simulation cell. This expression represents the formation of an MAB phase with an extended defect from elemental bulk precursor of constituent atoms, such as bcc Mo. The energetics of defect formation for MAlB are shown in Fig. 8. It should be noted that the energy difference between the different defect configurations is extremely small. The highest difference is approximately 0.05 eV per atom. A similar trend was obtained in the case of WAlB with similar energy differences between configurations. In both systems, we found the lowest formation energies mainly occur for defects with extended Al vacancies, such as Al-missed, inserted, and M_2AlB_2. However, it is worth noting that very small energy differences between configurations (on the order of a few meV/atom) implies that each of these configurations can equally likely form [46].

The calculated energetics for N_2AlB_2 systems are shown in Fig. 9. The energy difference between configurations is also small here, although unlike in the case of MAlB where a similar trend was observed for MoAlB and WAlB, here there is a marked difference in behavior for some of the structural defects. In particular, we found that while the NB-1 configuration (followed by NB-rot-2) is favored in

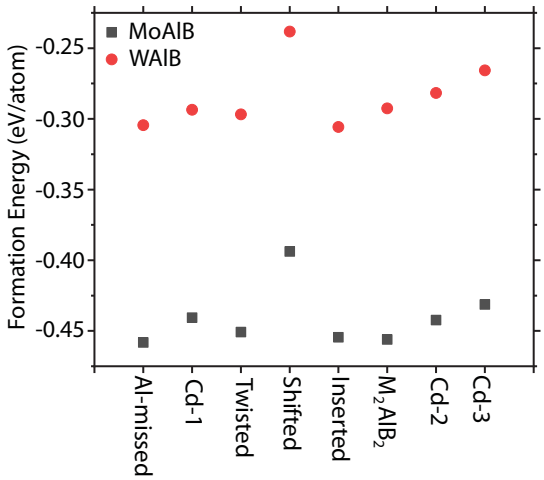

FIG. 8. Calculated formation energies of various structural defects in MoAlB and WAlB.

Cr_2AlB_2, the NB-Rot-1 configuration is favored in Fe_2AlB_2. This observation is in agreement with the experiment, where a stoichiometric NB-rot-2 type defect was observed [34]. Even though NB-rot-1 involves 90° rotation of one layer of NB, it disrupts the bonding environment as compared to the rest of the system. However, in NB-rot-2, all NB layers preserve the bonding environment as before the rotation. Our results are in line with experiments where the multiple CrB layers (likely even number of layers to minimize the formation energy) were rotated [34]. In the NB-2 configuration, the structural defect part contains a hexagonal arrangement of B atoms sandwiched between Cr atoms, which resembles Cr_2B_3 and the Cr-B subunit of Cr_3AlB_4. The latter compound has been already synthesized [3].

Equation (3) cannot be applied to determine the formation energy of extended defects that possess identical stoichiometry to that of the perfect crystal. Another way of assessing stability of stoichiometric extended defects is to utilize the following expression:

$$E_f^{\text{sto}} = \frac{E_{\text{defected}} - E_{\text{pristine}}}{A}, \tag{5}$$

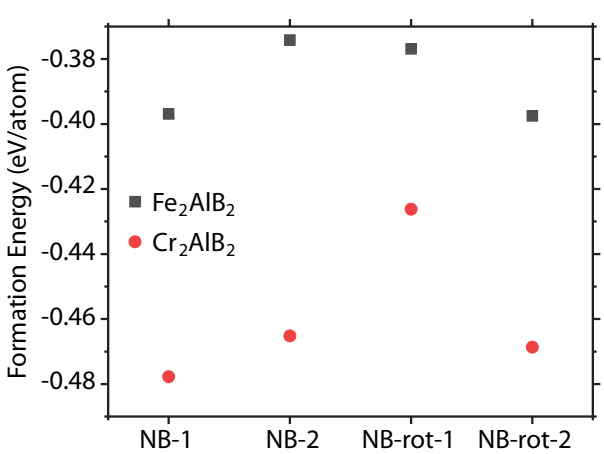

FIG. 9. Calculated formation energies of various structural defects in Cr_2AlB_2 and Fe_2AlB_2.

where E_{defected} is the total energy of the supercell with an extended defect, E_{pristine} is the total energy of the same number of formula units of perfect bulk crystal, and A is the cross-sectional area of the extended defect. E_f^{sto} is 10 meV/Å^2 for the twisted defect in MoAlB, and it becomes 9.3 meV/Å^2 for WAlB. The NB-rot-2 structure, a kind of twisted defect where two NB units are involved, has a very small formation energy of less than 1 meV/Å^2 in Cr_2AlB_2, meaning that this defect is very likely to form in line with experiment [34]. However, Fe_2AlB_2 exhibits a slightly higher value of 6.5 meV/Å^2. We also utilized Eq. (3) for the nonstoichiometric extended defects. When exposed to Al-deficient and Mo/B-rich conditions (i.e., point I on the phase diagram), the formation energies (E_f^{nonsto}) of extended nonstoichiometric defects such as Al-missing, Mo_2AlB_2-type, and inserted are −0.16 eV, −0.08 eV, and −0.50 eV, respectively. This means that these defects can spontaneously form under Al-poor conditions. On the other hand, Al-rich conditions lead to the formation energies that are positive and can range from 0.74 eV to as high as 2.58 eV. For other nonstoichiometric defects, E_f^{nonsto} varies between 0.89 and 1.84 eV. In the previous application of Eq. (3) for the extended defects, we changed the number of Mo and Al atoms while keeping the B atom concentration constant. In other words, we merely added and removed Mo and Al atoms in $Mo_{1\pm x}Al_{1\pm y}B$. However, for the inserted defect, E_f^{nonsto} becomes +2.58 eV at the point III, which corresponds to B/Mo-poor and Al-rich conditions. For Cr_2AlB_2, E_f^{nonsto} is negative for NB-1 at the points I, IV, V, and VI. However, NB-2 has a slightly negative formation energy at the points IV and V. The formation of NB-1 is always more favorable compared to NB-2. In contrast to MoAlB, the Al-missing and W_2AlB_2-type defects in WAlB exhibit positive formation energies of 0.02–0.42 eV and 0.42–0.82 eV, respectively, and it is very unlikely that a W_2AlB_2-type defect would occur regardless of the chemical potentials. However, at the point I on the phase diagram, the formation energy of an inserted defect is −1.30 eV, indicating a high likelihood of its formation. For all the chemical potentials considered, the NB-2 defect is unlikely in Fe_2AlB_2, despite its similar behavior to Cr_2AlB_2.

C. Grain boundaries

Grain boundaries (GBs) strongly affect a material's mechanical properties including hardness, brittleness, creep strength, corrosion resistance, fatigue strength, and weldability. In addition to the point and extended structural defects, we modeled the tilt grain boundary observed for Fe_2AlB_2 [34]. We also constructed the same grain boundary for Cr_2AlB_2 to compare these two MAB phases. Figure 10 shows this tilt boundary, where the boundary plane is (100) and the tilt axis is [010]. The tilt angle is approximately 31.80° as consistent with the experimental observation (29.78°). The grain boundary energy (γ_{GB}) is defined by the following expression,

$$\gamma_{GB} = \frac{E_{GB} - N_{GB}E_{\text{bulk}}}{2A_{GB}}, \tag{6}$$

where E_{GB} and N_{GB} are the total energy and number of atoms of the GB structure, respectively, A_{GB} is the cross-sectional area of the GB, E_{bulk} is the energy per atom of the bulk, and the

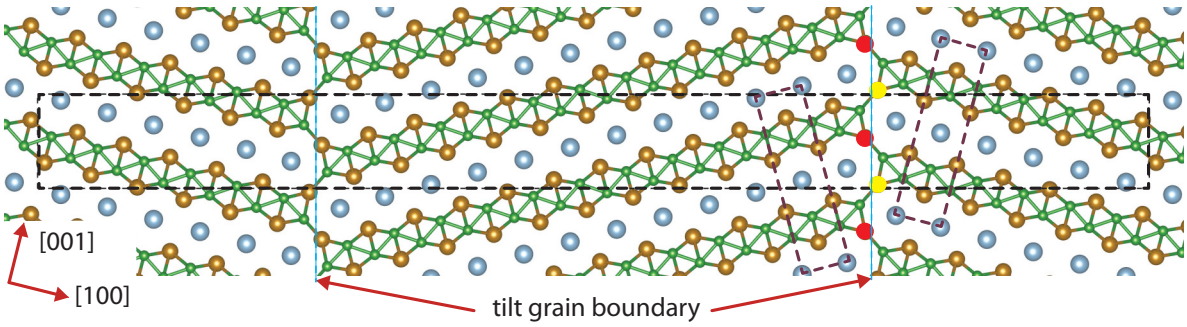

FIG. 10. A structural model of a tilt grain boundary. Black dashed lines enclose the simulation cell where two-grain boundaries are formed. Two brown dashed rectangles enclose conventional cell structures, which are tilted with respect to each other at the opposite sites of the grain boundary. Red (yellow) filled circles point out the Fe atoms at the right (left) side of the boundary.

factor of two in the denominator to take into account the two-grain boundaries present in our GB model. Based on above relation, γ_{GB} is found to be -0.002 for Fe_2AlB_2 and 0.002 eV/Å^2 for Cr_2AlB_2. It should be noted that GB for Fe_2AlB_2 has an unphysical negative γ_{GB} value that is very close to zero. This can be attributed to small numerical convergence errors. Here, we considered twin boundaries which are well known to have extremely small GB energies (on the order of 0.02 J/m^2 or 0.002 eV/Å^2), such as for fcc Sr, Ni, and Al [47,48].

To understand tilt grain boundary formation in Fe_2AlB_2 and not in Cr_2AlB_2, we computed surface energies for the (100) surface using the following expression,

$$\sigma_{\text{surf}} = \frac{E_{\text{surf}} - N_{\text{atoms}} E_{\text{bulk}}}{2A}, \tag{7}$$

where E_{surf} is the total energy of surface slab. E_{bulk} is the calculated total energy of bulk. A is the surface area. E_{surf} is 0.18 for Fe_2AlB_2 and 0.22 eV/Å^2 for Cr_2AlB_2, implying that the twin boundary formation is more likely in Fe_2AlB_2 in line with experimental observation [34]. In our grain boundary structure, the chemical environment (such as coordination numbers) of the Fe, Al, and B atoms is not too different than that in the pristine structures. The bond lengths as a function of distance from the boundary are quite similar with a variation of at most 0.1 Å. Fe_2AlB_2 has a ferromagnetic ground state where the magnetic moment for the Fe atom is 1.37 μ_B. The formation of the grain boundary changes the magnetic moments by at most 0.05 μ_B.

Another GB property is the work of separation W_{sep}, which is a measure of the energy required to cleave the GB into the free surfaces and is correlated to the fracture toughness. W_{sep} is given by the following expression,

$$W_{GB} = 2\sigma_{\text{surf}} - \gamma_{GB}, \tag{8}$$

where σ_{surf} is the corresponding surface energy for the facet (hkl) formed by cleaving the GB. As this equation points out, there is a negative correlation between GB energy and work of separation. W_{GB} becomes approximately 0.36 eV/Å^2 (or 5.77 J/m^2) for Fe_2AlB_2 by assuming a negligible grain boundary energy.

D. Defect migration

Table II shows the calculated diffusion barriers. We considered only vacancy migration as the migration of antisites will require exchange with a neighboring atom and it has been shown to be energetically unfavorable [14]. From the result obtained, V_{Al} possesses the lowest vacancy migration barrier in MoAlB and WAlB as compared to Cr_2AlB_2 and Fe_2AlB_2. The reason for this phenomenon can be explained by the presence of two layers of Al in MAlB, which creates an extra pathway for vacancy diffusion across these Al layers. According to ICOHP analysis, the covalent bond strength between Al atoms is generally weaker than that between Al-M (M = Mo and W) and Al-B. This weak bonding between Al atoms facilitates the easier movement of Al vacancies between the Al layers, as observed in the Supplemental Material [40].

However, V_B has the lowest diffusion barrier in Cr_2AlB_2 and Fe_2AlB_2. Our results show that the migration of Mo, W, Cr, and Fe is not favorable. Interestingly, the ease in the formation of V_B in all of the three systems does not translate to ease of migration. Nevertheless, the diffusion barrier values for V_B are significantly lower than those of V_M and comparable with that of V_{Al}. Within the transition state model, the defect's mobility is determined by the frequency of jumps between neighboring minimum energy sites via the following expression,

$$\nu = \nu_0 \exp\left(-\frac{E_b}{k_B T}\right), \tag{9}$$

where E_b is the migration barrier and ν_0 is the attempt frequency (see Fig. 11). The latter typically has a value $\sim 10^{12}$–10^{13} Hz and usually does not depend very critically on the type of defect. In contrast, different values of E_b for different defects easily result in ν varying by several orders

TABLE II. Calculated migration barrier of vacancies for MAlB and N_2AlB_2 in eV.

System	V_M	V_{Al}	V_B
MoAlB	5.39	0.45	0.66
WAlB	6.07	0.46	0.65
Cr_2AlB_2	4.68	2.17	0.72
Fe_2AlB_2	3.32	1.33	0.44

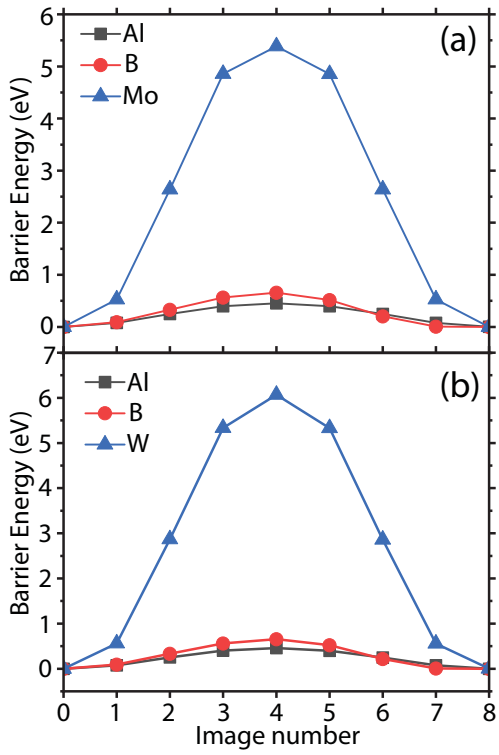

FIG. 11. Calculated vacancy migration barrier energies for (a) MoAlB and (b) WAlB.

of magnitude. Assuming an Arrhenius behavior with taking $\nu_0 = 10^{13}$ Hz, the attempt frequencies for vacancies are found and summarized in Table III. Our calculations lead to high hopping frequencies ν for the V_{Al} and V_B vacancies in MAlB in the range 10^9–10^{10} Hz at 1000 K. Transition metal atoms are barely mobile and mass transport in MAB phases occurs via Al and B vacancies.

Our calculated defect energetics provides a detailed insight into the behavior of these materials with respect to defect formation and migration. Materials used for high-temperature applications are expected to have temperature change resistance mechanisms. For instance, MAX compounds like Ti_3AlC_2 and Cr_2AlC exhibit resistance to thermal shock, and this behavior is attributed to energy-absorbing mechanisms which consume the thermal shock strain energy [49]. When there is a change in temperature leading to the surface cracks, the oxidation reaction is triggered, and Al_2O_3 layer forms. It was found that, in the MAX phase, when this occurs, the Al_2O_3 film fills the cracks, thereby enhancing the recovery strength of the material. A similar mechanism is accrued to the MAB phase, specifically for MoAlB. Our calculated migration energies show that V_{Al} is the easiest to migrate in MAlB systems, while they are not in N_2AlB_2 systems. We can here claim that the Al atoms migrate to the surface where the oxidation reaction takes place, and hence M and B locally form MB. The formed surface Al_2O_3 layer behaves as a protective layer and protects MAlB from further oxidation. This observation is in fact reported for MoAlB. Zhou *et al.* investigated the shock resistance capabilities of MoAlB by water quenching and found that the Al_2O_3 layer is formed by the mechanism described above [50]. They also reported that MoAlB has a better thermal shock resistance than Fe_2AlB_2, an observation that could be linked to the higher migration barrier of V_{Al} in Fe_2AlB_2. To strengthen our claim mentioned previously, we calculated Al vacancy formation energy as a function of position with respect to the surface layer of MoAlB. We only considered the two lowest energy surfaces, namely (010) and (111), of MoAlB. We found that creating Al vacancies on the surface of the (111) surface costs more energy as compared to those within subsurface layers by 0.25 eV for the first subsurface layer and 0.61 eV for the second subsurface Al layer. The vacancies migrate by interchanging with the nearest-neighbor ions in the lattice. In this respect, the Al vacancies (Al atoms) move deeply into (toward the surface of) MoAlB, which leads to the formation of nonstoichiometric $MoAl_{1-x}B$ domains. In a recent paper, the formation of a mesoporous α-MoB phase was demonstrated via a series of metastable intermediates including $MoAl_{1-x}B$, Mo_2AlB_2, and Mo_2AlB_2-AlO_x, which are ultimately derived from MoAlB. All of these steps involve the formation and migration of Al vacancies and stacking faults [51]. Furthermore, the simultaneous formation of structural extended defects and stacking faults in MAlB and N_2AlB_2 as described can be rationalized depending on the chemical potentials or experimental conditions. Indeed, a recent experiment already showed that some of these defects coexist with pristine structures [13]. The presence of excess point defects, such as Al vacancies, can lead to the formation of extended defects as they have a tendency to migrate relatively easily, for instance, in MoAlB.

TABLE III. Attempt frequencies (in Hz) calculated at 1000 K for vacancies.

System	V_{Al}	V_B
MoAlB	5.40×10^{10}	4.72×10^9
WAlB	4.81×10^{10}	5.30×10^9
Cr_2AlB_2	1.16×10^2	2.35×10^9
Fe_2AlB_2	1.98×10^6	6.06×10^{10}

One of the hallmarks of the MAB phases is their semblance to their binary borides. Interestingly, while our calculated defect formation and migration energetics depict similarities in MoAlB and WAlB, there are some evident differences in the defect behavior of Cr_2AlB_2 and Fe_2AlB_2. Notably, the calculated vacancy migration energies show marked difference in magnitude. Previously, it has been shown that while the formation of Cr_2AlB_2 is a result of high-temperature intercalation of Al atom between CrB layers, in the formation of Fe_2AlB_2, Al does not readily intercalate into the FeB structure [52]. A reconstructive reaction is required for the formation of Cr_2AlB_2. The formation and decomposition of Fe_2AlB_2 involve the formation of the Fe-Al intermetallic phases, supported by our calculation where relatively easy formation of the B vacancy facilitates the formation the Al antisite defect at the B site. This reaction combined with easy migration of the B vacancy gives rise to free B, which is hardly observed in XRD due to its amorphous nature [52].

Finally, as is known, the exfoliation of MAB phases into two-dimensional MBenes is extremely challenging. Comparing formation energies and diffusion barriers of Al and B

vacancies, one can realize that intact isolation of MB layers from MAB phases is unlikely due to the comparable energetics of these two defects.

IV. CONCLUSION

We calculated the defect formation energetics and migration in MoAlB, WAlB, Cr_2AlB_2, and Fe_2AlB_2. The aim is to provide insight into the behavior of both point and extended defects in these materials. Due to the significant impact that chemical potential has on the formation of defects, we first determined the limits of the chemical potentials to prevent the formation of competing phases. Our investigation revealed that chemical potential influences the formation of vacancy defects in MAlB more than in N_2AlB_2. For the vacancy defects, M/N vacancies are the least favorable in M/N-rich conditions. The dependence of the formation of antisite and interstitial defects on chemical potential in both classes of material is less pronounced. While the M interstitials are prohibitively expensive to be created in MAlB, they are more favorable in N_2AlB_2. Overall, in each of the systems, the vacancy and antisite defects form easier than interstitial ones. Furthermore, our investigation of the defect migration revealed that the Al vacancy is the easiest to migrate in MAlB but is more difficult in N_2AlB_2, and hence provided a basis for understanding the higher resistance capability of the MoAlB as compared to Fe_2AlB_2. We also investigated the stability of the different extended defects and stacking faults observed in each of the systems and obtained trends that are capable of guiding future synthesis of materials crystallizing in the MAB phase. We may achieve the formation of various extended defects and stacking faults depending on the experimental conditions. For instance, unlike MoAlB, the formation energies of the Al-missing and W_2AlB_2-type defects in WAlB are positive, ranging from 0.02–0.42 eV and 0.42–0.82 eV, respectively. Therefore, it is highly unlikely that a W_2AlB_2-type defect would form, regardless of the chemical potentials. Finally, we characterized a tilt grain boundary observed in N_2AlB_2. We related the grain boundary formation to the surface energetics, and found an easier formation tendency in Fe_2AlB_2 as opposite to Cr_2AlB_2 due to the lower surface energy in the former.

ACKNOWLEDGMENTS

This work is supported by the Air Force Office of Scientific Research under Award No. FA9550-21-1-0208. The computer resources used in this work are provided by the Computational Research Center at UND. Some of the computations were carried out at NDSU CCAST, which is supported by NSF Grants No. 1229316 and No. 2019077.

[1] S. Kota, M. Sokol, and M. W. Barsoum, A progress report on the MAB phases: Atomically laminated, ternary transition metal borides, Int. Mater. Rev. **65**, 226 (2020).

[2] M. W. Barsoum, The $M_{n+1}AX_n$ phases and their properties, in *Ceramics Science and Technology*, edited by R. R. Riedel and I.-W. Chen (Wiley, Weinheim, 2010), p. 299.

[3] M. Ade and H. Hillebrecht, Ternary borides Cr_2AlB_2, Cr_3AlB_4, and Cr_4AlB_6: The first members of the series $(CrB_2)_nCrAl$ with $n = 1, 2, 3$ and a unifying concept for ternary borides as MAB-phases, Inorg. Chem. **54**, 6122 (2015).

[4] M. Dahlqvist and J. Rosen, Chemical order or disorder: A theoretical stability expose for expanding the compositional space of quaternary metal borides, Mater. Adv. **3**, 2908 (2022).

[5] J. Wang, T.-N. Ye, Y. Gong, J. Wu, N. Miao, T. Tada, and H. Hosono, Discovery of hexagonal ternary phase Ti_2InB_2 and its evolution to layered boride TiB, Nat. Commun. **10**, 2284 (2019).

[6] M. Dahlqvist, Q. Tao, J. Zhou, J. Palisaitis, P. O. Persson, and J. Rosen, Theoretical prediction and synthesis of a family of atomic laminate metal borides with in-plane chemical ordering, J. Am. Chem. Soc. **142**, 18583 (2020).

[7] H. Stadelmaier, R. Burgess, and H. Davis, The ternary system Fe-Al-B, Metall. **20**, 225 (1966).

[8] P. J. Richardson, V. J. Keast, D. T. Cuskelly, and E. H. Kisi, Theoretical and experimental investigation of the W-Al-B and Mo-Al-B systems to approach bulk WAlB synthesis, J. Eur. Ceram. Soc. **41**, 1859 (2021).

[9] J. Y. Kim, J. Xi, H. Zhang, and I. Szlufarska, Defect chemistry of Cr-B binary and Cr-Al-B MAB phases: Effects of covalently bonded B networks, Phys. Rev. Mater. **5**, 113603 (2021).

[10] S. Kota, E. Zapata-Solvas, Y. Chen, M. Radovic, W. E. Lee, and M. W. Barsoum, Isothermal and cyclic oxidation of MoAlB in air from 1100 °C to 1400 °C, J. Electrochem. Soc. **164**, C930 (2017).

[11] L. Xu, O. Shi, C. Liu, D. Zhu, S. Grasso, and C. Hu, Synthesis, microstructure and properties of MoAlB ceramics, Ceram. Int. **44**, 13396 (2018).

[12] X. Lu, S. Li, W. Zhang, B. Yao, W. Yu, and Y. Zhou, Crack healing behavior of a MAB phase: MoAlB, J. Eur. Ceram. Soc. **39**, 4023 (2019).

[13] R. Sahu, D. Bogdanovski, J.-O. Achenbach, J. M. Schneider, and C. Scheu, Defects in an orthorhombic MoAlB MAB phase thin film grown at moderate synthesis temperature, Nanoscale **14**, 2578 (2022).

[14] H. Zhang, J. Y. Kim, R. Su, P. Richardson, J. Xi, E. Kisi, J. O'Connor, L. Shi, and I. Szlufarska, Defect behavior and radiation tolerance of MAB phases (MoAlB and Fe_2AlB_2) with comparison to MAX phases, Acta Mater. **196**, 505 (2020).

[15] H. Zhang, F.-Z. Dai, H. Xiang, X. Wang, Z. Zhang, and Y. Zhou, Phase pure and well crystalline Cr_2AlB_2: A key precursor for two-dimensional CrB, J. Mater. Sci. Technol. **35**, 1593 (2019).

[16] P. Rajpoot, A. Rastogi, and U. P. Verma, Insights into structural, electronic, optical and thermoelectric properties of WB and WAlB: A first principle study, Philos. Mag. **98**, 2657 (2018).

[17] M. Ali, M. Hossain, M. Uddin, A. Islam, D. Jana, and S. Naqib, DFT insights into new B-containing 212 MAX phases: Hf_2AB_2 (A = In, Sn), J. Alloys Compd. **860**, 158408 (2021).

[18] M. Hadi, N. Kelaidis, S. Naqib, A. Chroneos, and A. Islam, Mechanical behaviors, lattice thermal conductivity and vibrational properties of a new MAX phase Lu_2SnC, J. Phys. Chem. Solids **129**, 162 (2019).

[19] M. M. Ali, M. Hadi, M. Rahman, F. Haque, A. Haider, and M. Aftabuzzaman, DFT investigations into the physical properties of a MAB phase Cr_4AlB_4, J. Alloys Compd. **821**, 153547 (2020).

[20] P. A. Burr, D. Horlait, and W. E. Lee, Experimental and DFT investigation of $(Cr,Ti)_3AlC_2$ MAX phases stability, Mater. Res. Lett. **5**, 144 (2017).

[21] D. Horlait, S. C. Middleburgh, A. Chroneos, and W. E. Lee, Synthesis and DFT investigation of new bismuth-containing MAX phases, Sci. Rep. **6**, 18829 (2016).

[22] E. M. D. Siriwardane, R. P. Joshi, N. Kumar, and D. Çakır, Revealing the formation energy–exfoliation energy–structure correlation of MAB phases using machine learning and DFT, ACS Appl. Mater. Interfaces **12**, 29424 (2020).

[23] G. Kresse and J. Hafner, *Ab initio* molecular dynamics for liquid metals, Phys. Rev. B **47**, 558 (1993).

[24] G. Kresse and J. Hafner, *Ab initio* molecular-dynamics simulation of the liquid-metal–amorphous-semiconductor transition in germanium, Phys. Rev. B **49**, 14251 (1994).

[25] J. F. G. Kresse, Efficiency of *ab initio* total energy calculations for metals and semiconductors using a plane-wave basis set, Comput. Mater. Sci. **6**, 15 (1996).

[26] G. Kresse and J. Furthmüller, Efficient iterative schemes for *ab initio* total-energy calculations using a plane-wave basis set, Phys. Rev. B **54**, 11169 (1996).

[27] M. Ernzerhof and G. E. Scuseria, Assessment of the Perdew-Burke-Ernzerhof exchange-correlation functional, J. Chem. Phys. **110**, 5029 (1999).

[28] J. P. Perdew, K. Burke, and M. Ernzerhof, Generalized Gradient Approximation Made Simple, Phys. Rev. Lett. **77**, 3865 (1996).

[29] P. E. Blöchl, Projector augmented-wave method, Phys. Rev. B **50**, 17953 (1994).

[30] G. Kresse and D. Joubert, From ultrasoft pseudopotentials to the projector augmented-wave method, Phys. Rev. B **59**, 1758 (1999).

[31] E. M. D. Siriwardane, T. Birol, O. Erten, and D. Çakır, Nanolaminated Fe_2AB_2 and Mn_2AB_2(A = Al, Si, Ga, In) materials and the assessment of their electronic correlations, Phys. Rev. Mater. **6**, 124005 (2022).

[32] H. Jónsson, G. Mills, and K. W. Jacobsen, Nudged elastic band method for finding minimum energy paths of transitions, in *Classical and Quantum Dynamics in Condensed Phase Simulations* (World Scientific, Singapore, 1998), pp. 385–404.

[33] G. Henkelman, B. P. Uberuaga, and H. Jónsson, A climbing image nudged elastic band method for finding saddle points and minimum energy paths, J. Chem. Phys. **113**, 9901 (2000).

[34] J. Lu, S. Kota, M. W. Barsoum, and L. Hultman, Atomic structure and lattice defects in nanolaminated ternary transition metal borides, Mater. Res. Lett. **5**, 235 (2017).

[35] S. O. Akande and O. Bouhali, First-principles studies of defect behaviour in bismuth germanate, Sci. Rep. **12**, 15728 (2022).

[36] A. Jain, S. P. Ong, G. Hautier, W. Chen, W. D. Richards, S. Dacek, S. Cholia, D. Gunter, D. Skinner, G. Ceder *et al.*, Commentary: The Materials Project: A materials genome approach to accelerating materials innovation, APL Mater. **1**, 011002 (2013).

[37] Springer Materials, Landolt-Börnstein database, https://materials.springer.com.

[38] C. Shen, Q. Gao, N. M. Fortunato, H. K. Singh, I. Opahle, O. Gutfleisch, and H. Zhang, Designing of magnetic MAB phases for energy applications, J. Mater. Chem. A **9**, 8805 (2021).

[39] M. Khazaei, J. Wang, M. Estili, A. Ranjbar, S. Suehara, M. Arai, K. Esfarjani, and S. Yunoki, Novel MAB phases and insights into their exfoliation into 2D MBenes, Nanoscale **11**, 11305 (2019).

[40] See Supplemental Material at http://link.aps.org/supplemental/10.1103/PhysRevMaterials.7.053610 for the derivation and values of chemical potentials at different experimental conditions and the values of ICOHP for various bonds.

[41] J. Y. Kim, H. Zhang, R. Su, J. Xi, S. Wei, P. Richardson, L. Liu, E. Kisi, J. H. Perepezko, and I. Szlufarska, Defect recovery processes in Cr-B binary and Cr-Al-B MAB phases: Structure-dependent radiation tolerance, Acta Mater. **235**, 118099 (2022).

[42] V. L. Deringer, A. L. Tchougreeff, and R. Dronskowski, Crystal orbital Hamilton population (COHP) analysis as projected from plane-wave basis sets, J. Phys. Chem. A **115**, 5461 (2011).

[43] S. Maintz, V. L. Deringer, A. L. Tchougreeff, and R. Dronskowski, Analytic projection from plane-wave and PAW wavefunctions and application to chemical-bonding analysis in solids, J. Comput. Chem. **34**, 2557 (2013).

[44] S. Maintz, V. L. Deringer, A. L. Tchougréeff, and R. Dronskowski, LOBSTER: A tool to extract chemical bonding from plane-wave based DFT, J. Comput. Chem. **37**, 1030 (2016).

[45] Z.-K. Zhang, H. Gu, D.-D. Sun, Y.-L. Bai, and C.-F. Hu, Control of multiphase evolution and Al-deficiency in reactive-sintered MoAlB ceramics with excessive Al, J. Eur. Ceram. Soc. **42**, 5505 (2022).

[46] P. H. Mayrhofer, D. Music, and J. Schneider, Influence of the Al distribution on the structure, elastic properties, and phase stability of supersaturated $Ti_{1-x}Al_xN$, J. Appl. Phys. **100**, 094906 (2006).

[47] J. Li, S. J. Dillon, and G. S. Rohrer, Relative grain boundary area and energy distributions in nickel, Acta Mater. **57**, 4304 (2009).

[48] H. Zheng, X.-G. Li, R. Tran, C. Chen, M. Horton, D. Winston, K. A. Persson, and S. P. Ong, Grain boundary properties of elemental metals, Acta Mater. **186**, 40 (2020).

[49] S. Li, H. Li, Y. Zhou, and H. Zhai, Mechanism for abnormal thermal shock behavior of Cr_2AlC, J. Eur. Ceram. Soc. **34**, 1083 (2014).

[50] X. Lu, S. Li, W. Zhang, W. Yu, and Y. Zhou, Thermal shock behavior of a nanolaminated ternary boride: MoAlB, Ceram. Int. **45**, 9386 (2019).

[51] K. J. Baumler, L. T. Alameda, R. R. Katzbaer, S. K. O'Boyle, R. W. Lord, and R. E. Schaak, Introducing porosity into refractory molybdenum boride through controlled decomposition of a metastable Mo-Al-B precursor, J. Am. Chem. Soc. **145**, 1423 (2023).

[52] L. A. Hanner, S. Kota, and M. W. Barsoum, Formation mechanisms of Cr_2AlB_2, Cr_3AlB_4, and Fe_2AlB_2 MAB phases, Mater. Res. Lett. **9**, 323 (2021).